Effect of Reaction Atmosphere on Catalytic CO Oxidation Over Cu-Based Bimetallic Nanoclusters on a CeO_2 Support

Long Zhang,[1,2,*] Jing Pan,[1] Min Li,[1] Ivo A.W. Filot,[2] Emiel J.M. Hensen,[2,†] and Hui Wang[1,‡]

[1] *School of Physics, Hunan Key Laboratory of Super Microstructure and Ultrafast Process, Hunan Key Laboratory of Nanophotonics and Devices, State Key Laboratory of Powder Metallurgy, Central South University, Changsha 410083, China*

[2] *Department of Chemical Engineering and Chemistry, Eindhoven University of Technology, P.O. Box 513, 5600 MB Eindhoven, Netherlands*

(Received 2 April 2023; revised 17 August 2023; accepted 21 August 2023; published 21 September 2023)

Understanding the nature of active sites and the catalytic properties of oxide-supported bimetallic clusters under reaction conditions remains challenging. In this study, we combine first-principles calculations with genetic algorithm and grand canonical Monte Carlo methods to reveal the structures and compositions of CeO_2-supported Cu-based bimetallic clusters in an oxygen-rich environment. Oxidized Cu_4X_4 (X = Pd, Pt, and Rh) bimetallic clusters on $CeO_2(111)$ are stable and exhibit different catalytic properties during CO oxidation compared with the pristine bimetallic clusters. Microkinetic simulations predict that $CeO_2(111)$-supported $Cu_4Pd_4O_{10}$, $Cu_4Pt_4O_{11}$, and $Cu_4Rh_4O_{14}$ clusters have much higher CO oxidation activity than the supported Cu_4Pd_4, Cu_4Pt_4, and Cu_4Rh_4 clusters; this is ascribed to the moderate CO adsorption strength and active oxygen on oxidized alloy clusters. A mechanistic study suggests that CO oxidation occurs via the O_2 associative reaction mechanism on the $Cu_4Pd_4O_{10}$ and $Cu_4Pt_4O_{11}$ clusters, while it proceeds through the O_2 dissociative reaction mechanism on the $Cu_4Rh_4O_{14}$ cluster. Our calculations further predict that CO oxidation on the $Cu_4Rh_4O_{14}$ cluster exhibits a low apparent activation energy, indicating that the oxidized cluster possesses excellent CO oxidation activity. This work demonstrates that the catalytic activity and reaction mechanism vary with the composition and oxidation state of the alloy nanocluster under the reaction conditions and emphasizes the influence of the reaction atmosphere on the reaction mechanisms and catalytic activity of oxide-supported alloy catalysts.

DOI: 10.1103/PhysRevApplied.20.034051

I. INTRODUCTION

Oxide-supported metal clusters recently received great attention in heterogeneous catalysis due to their unique catalytic properties in many industrial reactions [1,2]. Unlike large metal-nanoparticle catalysts, supported metal clusters provide an alternative way to efficiently utilize metal atoms in catalytic processes. One of the remarkable advantages of nanocluster catalysts is their special structural and electronic properties [3,4]. Previous reports showed that nanoclusters were often more active than single-site catalysts for some important reactions, such as CO oxidation [5], NO reduction [6], CO_2 reduction [7], and dehydrogenation reactions [8], because the exposed atoms of a nanocluster with a suitable ensemble size could serve as a multisite active center. Especially, bimetallic nanocluster catalysts have exceptional activity, making them highly attractive for a wide range of applications in the field of heterogeneous catalysis [9–11]. The excellent catalytic activities are generally attributed to the catalytic synergistic effect between the two metal components of the catalyst, which can be further associated with the ligand and assembly effects of the bimetallic catalytic surface [12]. Bimetallic nanocluster catalysts are versatile systems with tunable structural and electronic properties that can be utilized to improve catalytic performance.

Fundamental studies of alloy catalysts were particularly focused on Cu-based [13], Pt-based [14], Pd-based [15], and Au-based alloy systems [16], due to their distinctive electronic structures and surface sites with respect to pure metal catalysts. Recently, CO oxidation on supported alloy catalysts has been extensively investigated because it is an important reaction in automotive catalytic converters and a prototypical reaction in model catalysis. Liu *et al*. reported

*L.zhang@csu.edu.cn
†E.J.M.Hensen@tue.nl
‡Huiwang@csu.edu.cn

that Au-Cu bimetallic nanoparticles supported by SBA-15 catalysts had a better CO oxidation performance than the supported monometallic Au or Cu nanoparticles [17]. The improved performance was ascribed to the formation of alloy-oxide islands on the substrate, which provided abundant active sites for the oxidation reaction. Using strong metal-support interactions between Pt-Co alloy and the oxide support, active lattice oxygen atoms were generated on Pt-Co/Co_3O_4-SiO_2, which resulted in exceptional catalytic performance in CO oxidation [18]. Similarly, the important role of the support was highlighted in tuning the catalytic performance of CO oxidation on the bimetallic Au-Cu/Al_2O_3 catalyst by controlling the formation of the active Au-CuO_x interface [19]. In this regard, oxide supports have a significant impact on the active sites and catalytic performance by influencing the bimetallic phase under reaction conditions.

Recently, ceria-supported alloy catalysts were extensively investigated due to their promising catalytic performance in various chemical reactions [20–22]. By combining kinetic analysis with *in situ* diffuse reflectance IR spectroscopy studies, Liao *et al*. reported that the reduced Au-Cu/CeO_2 catalysts were more active toward the preferential CO oxidation than the calcined samples [23]. The promoting effect of alloying on the CeO_2-supported Au-Cu catalyst is reflected by the fast kinetic process of oxygen activation on gold-alloyed copper sites. It is not surprising that the amount of metal loading and the ratio of Pt and Au have an impact on the catalytic performance of Pt-Au/CeO_2 catalysts [24]. In fact, the catalytic activity is also affected by the size of alloy clusters [25]. Small clusters supported on oxides have a unique atomic coordination environment and exhibit different catalytic properties compared with large nanoparticles [5]. For example, the reactants do not compete for adsorption sites on the CeO_2-supported Au-Cu alloy cluster, which is crucial for the excellent performance of CO oxidation [26]. A detailed mechanistic study indicated that catalytic oxidation of CO over Cu_3Pt_7 and Cu_3Rh_7 supported on ceria occurred via two different mechanisms, namely, the O_2 associative and dissociative reaction pathways [27]. A computational study of the $CeO_2(111)$-supported Pd-based alloy catalyst suggested that the Pd-Ag/CeO_2 interface facilitated CO oxidation via the Mars-van Krevelen mechanism [28]. However, the catalytic models constructed in previous studies did not reflect the influence of the reaction atmosphere on CO oxidation. In fact, the adsorbed O_2 molecules on alloy clusters rapidly dissociate into oxygen adatoms, which leads to the restructuring of the geometric and electronic structure of supported metals during CO oxidation. In other words, the actual state of the supported nanocluster is related to the reaction atmosphere, which poses a challenge for resolving the structure and identifying the active site of the supported alloy catalyst. As our previous work indicated, the oxidation state of the Pd cluster on ceria had an impact on the kinetics of CO oxidation on the catalytic surface [29]. Similar to supported Pd catalysts, the reaction rates of CO oxidation on ceria-supported Au clusters vary, depending on the oxidation state of the supported gold cluster. This oxidation state strongly depends on the ceria support and the reaction environment [30]. However, there is a lack of computational studies for understanding the catalytic properties of CeO_2-supported bimetallic clusters under the reaction conditions of CO oxidation.

Here, we employ methods rooted in first-principles-based genetic algorithm (GA) and grand canonical Monte Carlo (GCMC) simulations to determine the most stable structures of Cu-based alloy clusters placed on a $CeO_2(111)$ surface under typical reaction conditions. Based on density functional theory (DFT) computed energy profiles of CO oxidation reaction pathways on optimized structures, we carry out microkinetic analysis and find that the reaction mechanisms for CO oxidation on ceria-supported oxidized Cu_4X_4 ($X =$ Pd, Pt, and Rh) alloy catalysts are governed by the composition and oxidation state of the alloy clusters. The reaction is more likely to take place on oxidized Cu-based bimetallic clusters rather than at the interface. The oxidized alloy clusters exhibit much higher activity for CO oxidation compared to their metallic counterparts. This is attributed to the higher oxidation state of the oxidized Cu-based alloy clusters, resulting in moderate CO adsorption strength and a lower energy barrier for CO_2 formation. Particularly, the $CeO_2(111)$-supported oxidized Cu_4Rh_4 cluster exhibits superior catalytic activity in CO oxidation. Our findings provide insights into understanding the nature of active sites and catalytic properties of ceria-supported Cu-based bimetallic clusters in an oxygen-rich environment.

II. COMPUTATIONAL METHODS

We employed spin-polarized DFT calculations using the projector-augmented-wave [31] approach, as implemented in VASP 5.4.4 [32,33]. To consider the effect of exchange correlation and on-site coulomb interactions, the Perdew-Burke-Ernzerhof [34] functional with the Hubbard $+ U$ correction was adopted. A U_{eff} value of 4.5 eV for Ce was considered based on a previous study [35]. We used a cutoff energy of 400 eV for constructing the valence-electron density in the plane-wave basis. Structure optimization was stopped when Hellmann-Feynman forces acting on atoms were less than 0.02 eV/Å. For the ceria support, a stable $CeO_2(111)$ surface with a 4×4 unit cell and six atomic layers was constructed. Here, the top-three layers were relaxed, and the bottom-three layers were fixed. A vacuum thickness of 12 Å was used to avoid interactions between periodic images along the z direction. Since the constructed unit cells were large enough, a Monkhorst-Pack k point of $1 \times 1 \times 1$ was

used for the Brillouin-zone integration. To calculate the energy barriers for surface reactions, the transition states were searched using the climbing-image nudged-elastic-band method [36]. The structure of the transition state was determined by vibrational-frequency analysis with a single mode of imaginary frequency in the direction of the reaction coordinate.

To model ceria-supported Cu-based alloy catalysts, Cu_4Pd_4, Cu_4Pt_4, and Cu_4Rh_4 bimetallic clusters placed on $CeO_2(111)$ were considered. The global energy-minimum structure of ceria-supported alloy clusters were determined by DFT + GA. The computational framework for structure searches started with an initial population of 12 randomly generated structures. Three typical operations, namely, crossover, mutation, and selection, were considered in the evolutionary process to iteratively update the population pool. To mimic natural selection, two structures in the population were selected as parents to reproduce offspring if their fitness values exceeded a random number threshold. Each of the parent clusters was divided into two fragments, referred to as the "left" and "right" genes, by a randomly oriented plane passing through the mass center of each parent. The generated structure, known as the infant cluster, was produced by splicing the left and right genes from the parents under the restriction of the stoichiometry of a cluster containing N atoms. The new candidate structures were generated by repeating the above crossover step. Typically, a stable structure could be obtained within 30 iterations and less than 300 structure optimizations during GA calculations. The optimized structure with the lowest total energy among the candidates was determined as the most stable structure of $Cu_4X_4/CeO_2(111)$. To explore the state of $Cu_4X_4/CeO_2(111)$ in an oxygen environment, DFT + GCMC simulations were carried out. In the DFT + GCMC computational framework, three operations, namely, insertion of an oxygen at a random site, deletion of a randomly selected oxygen atom, and displacement of an oxygen atom on clusters, were employed. New structures generated from each operation were optimized by DFT calculations to obtain the total energy, followed by considering an acceptance criterion for the trial move based on the Boltzmann distribution [37,38]. The probability of accepting O insertion, deletion, and translation during the MC transition can be determined by the following acceptance criteria:

$$P_{\text{deletion}} = \min\left[1, \frac{N\Lambda^3}{V} exp[-\beta(\mu_{\text{res}} + E_n - E_o)]\right], \tag{1}$$

$$P_{\text{insertion}} = \min\left[1, \frac{V}{(N+1)\Lambda^3} exp[\beta(\mu_{\text{res}} - E_n + E_o)]\right], \tag{2}$$

$$P_{\text{translation}} = \min[1, \exp[-\beta(E_n - E_o)], \tag{3}$$

where N represents the number of O atoms in the system before the MC move; V and Λ stand for the system volume and the thermal de Broglie wavelength of the exchangeable particle, respectively. β is the Boltzmann factor calculated by $\beta = 1/k_BT$, where k_B is the Boltzmann constant. E_n and E_o are the total energies for the new and old configurations, respectively. μ_{res} is the chemical potential of the O_2 reservoir, which is calculated by

$$\mu_{\text{res}} = \frac{1}{2}\left[\mu_{O_2}(T, P^0) + k_B T \ln\left(\frac{P_{O_2}}{P^0}\right) - E_t\right], \tag{4}$$

where $\mu_{O_2}(T, P^0)$ is the standard chemical potential of O_2 at T and P^0, which can be obtained from the NIST JANAF thermochemical table [39]; E_t is the total energy of an isolated O_2 molecule. After enough trial iterations, no more new structures were found and the final structure was determined to be an equilibrium structure in the reactant environment. The converged system shows the formation of an oxide cluster at equilibrium with gas-phase O_2 at the temperature and pressure specified by the reference chemical potential. A detailed description of the DFT-based GA and GCMC simulations can be found in previous work [40].

Based on the DFT-computed energy profiles, we employed microkinetic simulations to explore the kinetic properties for CO oxidation on $CeO_2(111)$-supported Cu-based bimetallic clusters. The rate of the overall reaction, the rate-determining step, and coverage distribution were investigated in our simulations. For the CO_2-formation process, the calculated energy barriers were used to estimate the forward and backward rate constants for the surface reaction using the Eyring equation:

$$k = \frac{k_B T}{h} \frac{f^{\text{TS}}}{f} e^{-(E_a/k_B T)}, \tag{5}$$

where k is the reaction rate constant, k_B and h are the Boltzmann and Planck constants, respectively; T indicates the temperature; and E_a represents the energy barrier for the surface reaction. f^{TS} and f stand for the partition functions of the transition state and the ground state, respectively. In our simulations, all vibrational partition functions were assumed to be unity, which gave a prefactor for surface elementary reaction steps of about 10^{13} s^{-1}.

For the reactant-adsorption process, we assume that the molecule loses only one of its translational degrees of freedom with respect to the gas phase. Therefore, the rate of reactant adsorption is calculated by

$$r_{\text{ads}} = \frac{PA}{\sqrt{2\pi m k_B T}} S, \tag{6}$$

where P is the pressure of the reactant in the gas phase, A is the surface area of the adsorption site, and m refers to the

mass of the adsorbate. S indicates a dimensionless sticking coefficient.

For the CO_2 desorption step, there is an assumption that the formed species has two translational and three rotational degrees of freedom. Accordingly, the molecular desorption rate is calculated by [40]

$$r_{\mathrm{des}} = \frac{k_B T^3}{h^3} \frac{A(2\pi m k_B)}{\sigma \theta_{\mathrm{rot}}} e^{-(E_{\mathrm{des}}/k_B T)}, \tag{7}$$

where σ, θ, and E_{des} stand for the symmetry number, the characteristic temperature for rotation, and the desorption energy, respectively. The symmetry number of CO is 1. The symmetry numbers of O_2 and CO_2 are both 2. The characteristic temperatures of rotation for CO, O_2, and CO_2 are 2.73, 2.08, and 0.56 K, respectively [41].

To determine the reaction rate of all surface reaction intermediates, the differential equations were constructed by using the rate constants of the elementary reaction steps. For a system of N elementary reaction steps, there are $2N$ rate expressions for forward and backward reactions. The reaction rate can be expressed as [42]

$$r_j = k_j \prod_i c_i^{\nu_i^j}. \tag{8}$$

In Eq. (8), k_j indicates the elementary reaction rate constant, ν_i^j is the stoichiometric coefficient of component i in elementary reaction step j, and c_i is the concentration of component i on the catalytic surface. The above expressions were employed to derive an ordinary differential equation for each component on the catalyst with the form

$$\frac{dc_i}{dt} = \sum_j \nu_{i,j} r_j, \tag{9}$$

where c_i represents the dimensionless concentration of species i on the catalyst, and $\nu_{i,j}$ is the dimensionless stoichiometric coefficient of species i in elementary reaction step j.

The rate-determining step of the CO oxidation reaction on the catalyst was determined with the Campbell's degree of rate control (DRC) analysis [43,44]. For a specific elementary step i, the coefficient of the DRC ($\chi_{\mathrm{RC},i}$) is calculated by

$$\chi_{\mathrm{RC},i} = \frac{k_i}{r}\left(\frac{\partial r}{\partial k_i}\right)_{k_{j\neq i}, K_i} = \left(\frac{\partial \ln r}{\partial \ln k_i}\right)_{k_{j\neq i}, K_i}. \tag{10}$$

Here, r indicates the overall reaction rate, k_i is the forward rate, and K_i is the equilibrium constant for step i.

The DFT-based microkinetic simulations for CO oxidation on $Cu_4X_4/CeO_2(111)$ and $Cu_4X_4O_n/CeO_2(111)$ were employed using the MKMCXX code [45]. The reaction rates of CO_2 formation, degree of rate control, and steady-state coverages were calculated as a function of temperature by integrating the ordinary differential equations with respect to time using the backward differentiation formula method [46–48].

III. RESULTS AND DISCUSSION

Identifying the actual state of the catalyst under the reaction conditions is crucial for understanding the nature of its active sites and catalytic properties. In this study, we determined the global energy-minimum structure of $CeO_2(111)$-supported Cu_4X_4 bimetallic clusters by employing a structure evolutionary method based on genetic algorithm and first-principles calculations. Here, DFT calculations were carried out, mostly to obtain the total energy and characteristics of the optimized structure. Using this computational framework, we successfully predicted the most stable structure of the ceria-supported Au nanocluster, as shown in our previous study [30]. We extend the above method by mixing two metallic components in a model cluster for the optimization of a supported alloy catalyst. Figures 1(a)–1(c) show the lowest-energy structures of $CeO_2(111)$-supported Cu_4X_4 clusters. The supported alloy clusters adopt bilayer structures, which are in line with previous observations that identify bilayer structures for oxide-supported metal catalysts [49–51]. For Cu_4Pd_4/CeO_2 and Cu_4Pt_4/CeO_2, all the Cu atoms are located at the bottom of the cluster and bind with the surface lattice oxygen. The location of the Cu atoms in Cu_4Rh_4/CeO_2 is different and only one Cu atom is located at the top layer of the cluster and the rest of the Cu atoms are at the bottom of the cluster. It is not surprising that the local coordination environment of these supported clusters is different due to the different intrinsic properties of the metals and metal-support interaction. Additionally, the strong interaction between the surface O atoms of ceria and metal atoms induces strain within the clusters. Clearly, the strong interaction is reflected by the distribution of partial density of states (PDOS) for the bottom metal d states and surface O p states in Cu_4X_4/CeO_2, as displayed in Fig. S1 within the Supplemental Material [52]. We clearly observe a significant overlap between the metal d states of the cluster and the surface O p states, indicating a strong interaction between the cluster and ceria. This interaction also serves to stabilize and shape the bimetallic cluster.

To unravel the active site and catalytic properties in terms of shape and chemical composition in ceria-supported Cu-based alloy catalysts in an oxygen-rich environment, we employed a first-principles-based GCMC approach to predict the structures of $CeO_2(111)$-supported Cu-based alloy clusters by considering the effect of reactant (O_2) pressure and reaction temperature. In this grand

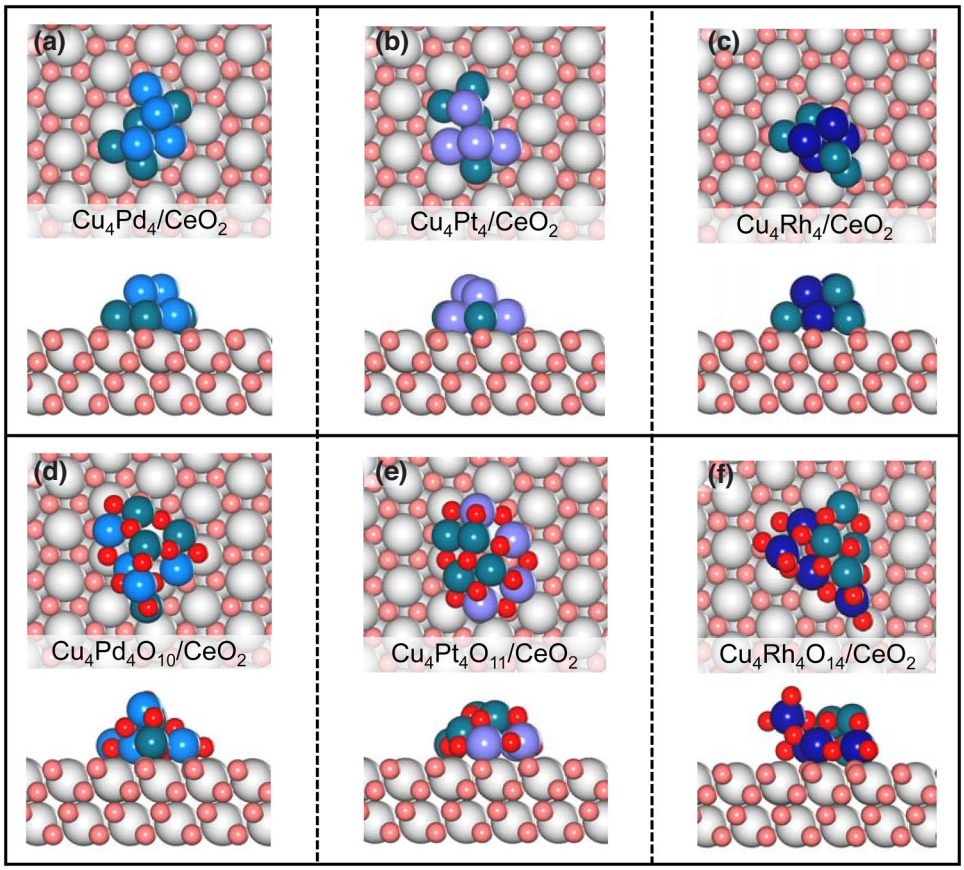

FIG. 1. (a)–(c) Structures of $CeO_2(111)$-supported Cu_4X_4 (X = Pd, Pt, and Rh) (structures optimized by GA + DFT), (d)–(f) structures of $CeO_2(111)$-supported $Cu_4X_4O_n$ (structures obtained by GCMC + DFT at 300 K under an oxygen atmosphere of 1 atm). (Color code: gray, Ce; pink or red, O; cyan, Cu; blue, Pt; light blue, Pt; deep blue, Rh.)

canonical approach, we adopted trial steps (insertion, deletion, and translation) based on the Metropolis algorithm, in which we considered the Gibbs free energy, $\mu(T, P)$, of existing and trial structures. Here, the Gibbs free energy is calculated by taking into account the total electronic energy of the catalyst and the Gibbs free energy of the gaseous O_2 reservoir. Considering the concentration of CO is generally much lower compared to that of O_2 during catalytic tests for CO oxidation, the impact of CO on the oxidation state of the metal cluster is negligible. Therefore, our DFT-based GCMC simulations can be simplified by accounting for compositional changes using an O_2 reservoir at a specific pressure (1 atm) and temperature (300 K). Using this approach, we predicted that the $Cu_4Pd_4O_{10}$, $Cu_4Pt_4O_{11}$, $Cu_4Rh_4O_{14}$ clusters on $CeO_2(111)$ would be stable under oxygen-rich conditions [Figs. 1(d)–1(f)]. Compared to supported Cu_4X_4, the Cu atoms of oxidized clusters tend to be located at the second layer of the clusters. Under oxidation reaction conditions, the oxidation states and morphologies of supported alloy clusters vary significantly, depending on the metal component. Generally, the activity of the catalyst is governed by its geometric and electronic structure; thus, the oxidized alloy cluster, under the reaction conditions, will exhibit very different catalytic performance from that of the metallic clusters.

To explore the catalytic properties of ceria-supported Cu_4X_4 and $Cu_4X_4O_n$ clusters, we investigate the reaction mechanism of CO oxidation starting from an understanding of CO adsorption behavior. Generally, an adsorption site with a more negative adsorption energy of CO is more likely to capture CO and initiate the subsequent reaction. Through a comparison of the adsorption energies for CO on typical sites (e.g., bridge, hollow, and top sites) of Cu_4X_4 clusters (Table S1 within the Supplemental Material [52]), we can determine the most favorable site for CO adsorption on the cluster. For CO adsorption on $Cu_4X_4O_n/CeO_2$, we identified the most favorable adsorption site by comparing the adsorption energies of CO on coordinately unsaturated Cu and X atoms of $Cu_4X_4O_n/CeO_2$ (Table S2 within the Supplemental Material [52]). For the first CO adsorption on Cu_4Pd_4/CeO_2, CO prefers to bind with the Pd-Cu bridge site with an adsorption energy of −2.14 eV, as shown in

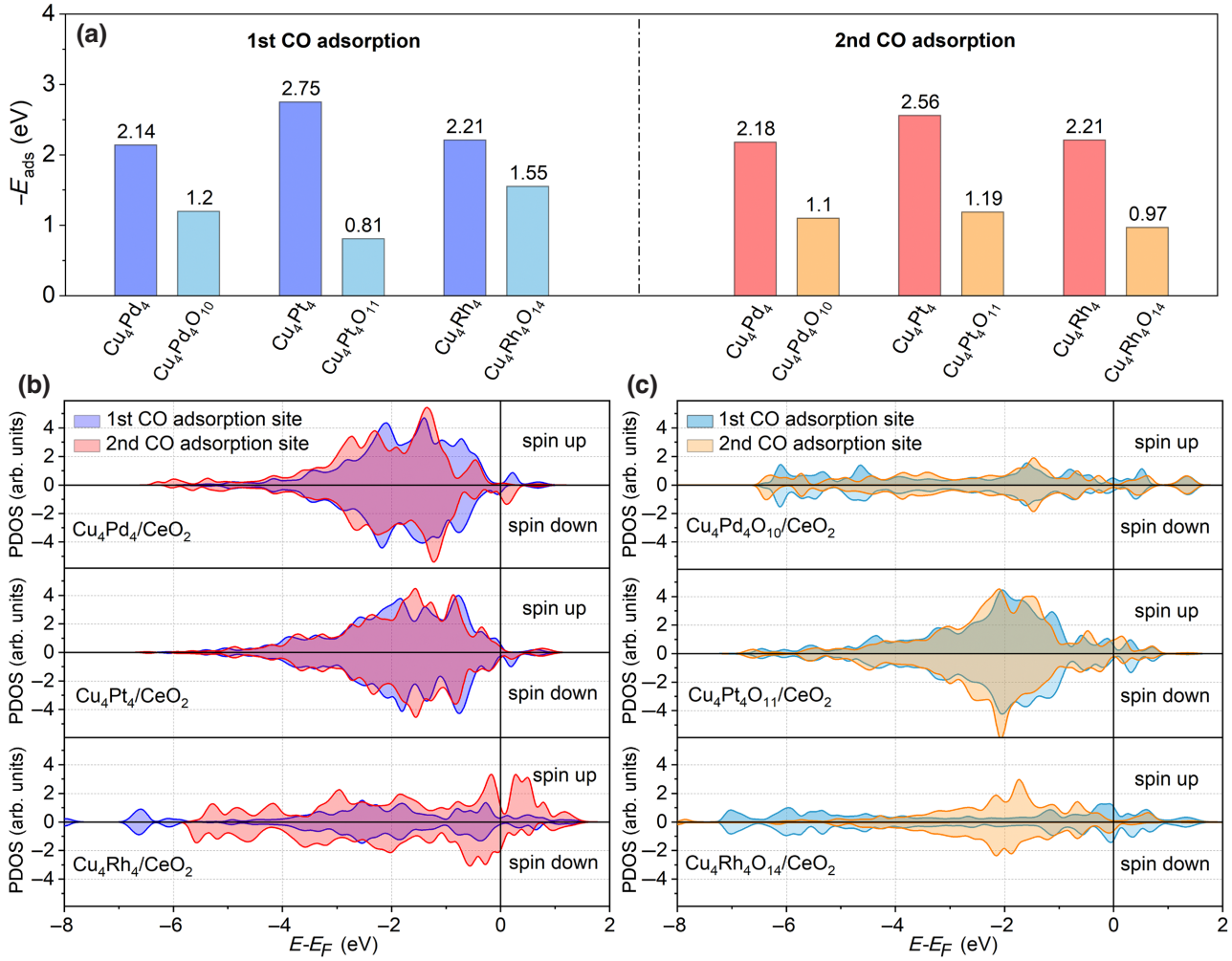

FIG. 2. (a) Adsorption energies for the first and second CO adsorptions on Cu_4X_4/CeO_2 and $Cu_4X_4O_n/CeO_2$, (b) PDOS analysis on *d* states of the metal atoms in the first and second CO adsorption sites of Cu_4X_4/CeO_2, (c) PDOS analysis on *d* states of the metal atoms in the first and second CO adsorption sites of $Cu_4X_4O_n/CeO_2$. These PDOS figures are plotted for the bimetallic clusters without CO adsorption. First and second adsorption sites represent specific metal atoms within the clusters binding to the first and second CO molecules, respectively.

Fig. 2(a) and Fig. S2 within the Supplemental Material [52]. Compared to CO adsorption on Cu_4Pd_4/CeO_2, CO binds more strongly to Cu_4Pt_4/CeO_2 ($E_{ads}=-2.75$ eV) and Cu_4Rh_4/CeO_2 ($E_{ads}=-2.21$ eV). After the desorption of formed CO_2 from the catalytic surface, the second CO adsorption is essential to close the overall catalytic cycle. We calculated the second CO adsorption energies, i.e., −2.18 eV (Cu_4Pd_4/CeO_2), −2.56 eV (Cu_4Pt_4/CeO_2), and −2.21 eV (Cu_4Rh_4/CeO_2), which were comparable to the first CO adsorption on the corresponding clusters. The adsorption behavior of CO on supported $Cu_4X_4O_n$ clusters is different, as shown in Fig. 2(a) and Fig. S2 within the Supplemental Material [52]. The first CO adsorption energies for $Cu_4Pd_4O_{10}/CeO_2$, $Cu_4Pt_4O_{11}/CeO_2$, and $Cu_4Rh_4O_{14}/CeO_2$ are −1.20, −0.81, and −1.55 eV, respectively. Similarly, the second CO adsorption for oxidized alloy clusters exhibit adsorption energies of −1.10 eV ($Cu_4Pd_4O_{10}/CeO_2$), −1.19 eV ($Cu_4Pt_4O_{11}/CeO_2$), and −0.97 eV ($Cu_4Rh_4O_{14}/CeO_2$). Clearly, the adsorption strength for the first and second CO oxidation on the oxidized alloy clusters are both much weaker than those on the corresponding metallic clusters.

The different behaviors of CO adsorption on ceria-supported Cu_4X_4 and $Cu_4X_4O_n$ clusters are investigated by conducting the PDOS analysis of relevant catalytic models. As CO interacts with metal atoms belonging to adsorption sites in the cluster, wave-function matching between the molecular orbital of CO and the *d* orbitals of the metal atoms becomes important. It is clear that the adsorption sites of Cu_4X_4 clusters have more *d* states available for bonding with CO in comparison to the

adsorption sites of $Cu_4X_4O_n$ clusters [Figs. 2(b) and 2(c)]. The nonbonding *d* states in Cu_4X_4 clusters are more favorable for interacting with CO orbitals, resulting in substantial electron donation to the adsorbate and an enhanced adsorption strength of CO. Additionally, we find that the band widths of the *d* bands on $Cu_4X_4O_n$ are broader than those for the corresponding Cu_4X_4 clusters. This is because the metal atoms are coordinated with oxygen atoms, leading to a stronger interaction between *d* states of the metal atom and *p* states of the adsorbed oxygen atoms. Compared to Cu_4X_4, the relatively broad *d* bands and low-energy positions of the *d*-band centers in oxidized $Cu_4X_4O_n$ are observed. As a result, electron donation from the oxidized metal atom to adsorbed CO would be reduced, leading to a significant decrease of the adsorption strength of CO on $Cu_4X_4O_n$ clusters. This is supported by the PDOS of C *p* states of adsorbed CO and transition-metal (TM) *d* orbitals of the metal atoms in adsorption sites (Figs. S3 and S4 within the Supplemental Material [52]). Clearly, the overlap between the C *p* and TM *d* states in CO adsorbed on Cu_4X_4/CeO_2 clusters is more pronounced compared to CO adsorbed on $Cu_4X_4O_n/CeO_2$ clusters. Additionally, the energy positions of the overlap between C *p* and TM *d* states in CO adsorbed on Cu_4X_4/CeO_2 are lower than those in CO adsorbed on $Cu_4X_4O_n/CeO_2$. These results suggest that the *p*-*d* orbital hybridization between the C and TM atoms in CO adsorbed on metallic Cu_4X_4 clusters is stronger than that in CO adsorbed on the oxidized clusters. As a result, the adsorption strength for CO on Cu_4X_4/CeO_2 is much stronger than that for CO on $Cu_4X_4O_n/CeO_2$. The above results show that the reaction atmosphere has a profound effect on the oxidation states of the supported alloy cluster, resulting in different CO adsorption properties. In light of the Sabatier principle, we expect that the CO oxidation performance will benefit from the moderate adsorption strengths of CO.

In the reaction mechanisms discussed below, we first adopt a Langmuir-Hinshelwood (L-H) mechanism, which implies that adsorbed CO reacts with adsorbed O_2 to produce CO_2 on Cu_4X_4/CeO_2. After CO adsorption, molecular oxygen adsorbs on the alloy cluster close to the CO molecule. The adsorption energies of O_2 on Cu_4Pd_4, Cu_4Pt_4, and Cu_4Rh_4 clusters are -1.09, -0.83, and -2.20 eV, respectively. The O_2 adsorption strength on alloy clusters is weaker than the CO adsorption strength. Then, CO oxidation via the O_2 dissociative and associative mechanisms is explored. In the O_2 dissociative mechanism, O_2 first dissociates into two O adatoms, where the atoms adsorb on the different Pd sites of the Cu_4Pd_4 cluster, as shown in Fig. 3(a). Similar to O_2 dissociation on Cu_4Pd_4, the O atoms tend to bind with Pt sites of the Cu_4Pt_4 cluster [Fig. 3(b)]. For the Cu_4Rh_4 cluster, the O atoms prefer to adsorb on the Cu-Rh bridge site [Fig. 3(c)]. The O_2 dissociative step on Cu_4Pd_4 and Cu_4Pt_4 are both thermodynamically and kinetically feasible, with energy barriers of 0.06 and 0.16 eV, respectively. This step is relatively difficult on Cu_4Rh_4/CeO_2 with a higher energy barrier (0.90 eV). Subsequently, adsorbed CO reacts with the O adatom on the cluster and forms CO_2, as shown in Fig. 3. This step is exothermic on Cu_4Pd_4/CeO_2 with a low energy barrier of 0.15 eV. This process becomes endothermic and requires high energy barriers on Cu_4Pt_4/CeO_2 (1.82 eV) and Cu_4Rh_4/CeO_2 (2.12 eV) to be overcome. In the O_2 associative mechanism, adsorbed CO directly reacts with adsorbed O_2 and forms the $OCOO^*$ intermediate. We find there is an energy barrier of 0.83 eV for this step on Cu_4Pd_4/CeO_2, which is apparently higher than that of CO_2 formation via the O_2 dissociative mechanism. On the contrary, the formation of the $OCOO^*$ intermediate on Cu_4Pt_4/CeO_2 and Cu_4Rh_4/CeO_2 has lower barriers than those for CO_2 formation via the O_2 dissociative mechanism, as shown in Figs. 3(a)–3(c) and Figs. S5(a)–S5(c) within the Supplemental Material [52]. Furthermore, our calculations indicate that the dissociation of $OCOO^*$ on all the clusters is facile, as characterized by low energy barriers. This ease of dissociation can be attributed to the interaction between CO and adsorbed O_2, which activates the bond of the O_2 species and facilitates the dissociation of $OCOO^*$. Therefore, CO oxidation on Cu_4Pd_4/CeO_2 via the O_2 dissociative pathway is more favorable than the O_2 associative pathway. The reaction pathway involved in the O_2 associative step is dominant for CO oxidation on Cu_4Pt_4/CeO_2 and Cu_4Rh_4/CeO_2. On the other hand, CO oxidation at the interface of Cu_4X_4/CeO_2 is investigated, as shown in Fig. S6 within the Supplemental Material [52]. The reaction of adsorbed CO with the nearest lattice oxygen at the interfaces of Cu_4Pd_4/CeO_2, Cu_4Pt_4/CeO_2, and Cu_4Rh_4/CeO_2 requires energy barriers of 2.21, 3.07, and 2.20 eV, respectively, to be overcome. The high energy barriers for the reaction at Cu_4X_4/CeO_2 interfaces indicate that CO prefers to react with oxygen atoms on alloy clusters rather than the ones from the ceria surface. Therefore, our study focuses on CO oxidation over alloy clusters. The second CO oxidation on the supported Cu_4Pd_4 cluster encounters a significantly higher energy barrier of 1.86 eV compared to the first CO oxidation. In contrast, lower energy barriers are found for the second CO oxidation on Cu_4Pt_4/CeO_2 (1.80 eV) and Cu_4Rh_4/CeO_2 (1.48 eV). After the formation of CO_2 species, CO_2 immediately desorbs from the clusters and produces gas-phase CO_2.

The performance of the catalyst in CO oxidation generally depends on the adsorption strength of CO and O_2. Reshaping supported Cu-based alloy clusters under the reaction condition weakens the CO adsorption, which has a significant impact on the catalytic activity. Since coadsorption of CO and O_2 on supported $Cu_4X_4O_n$ clusters are not feasible, we exclude the L-H reaction mechanism for CO oxidation on the oxidized clusters. Instead, the reaction pathway via the Mars-van Krevelen mechanism for

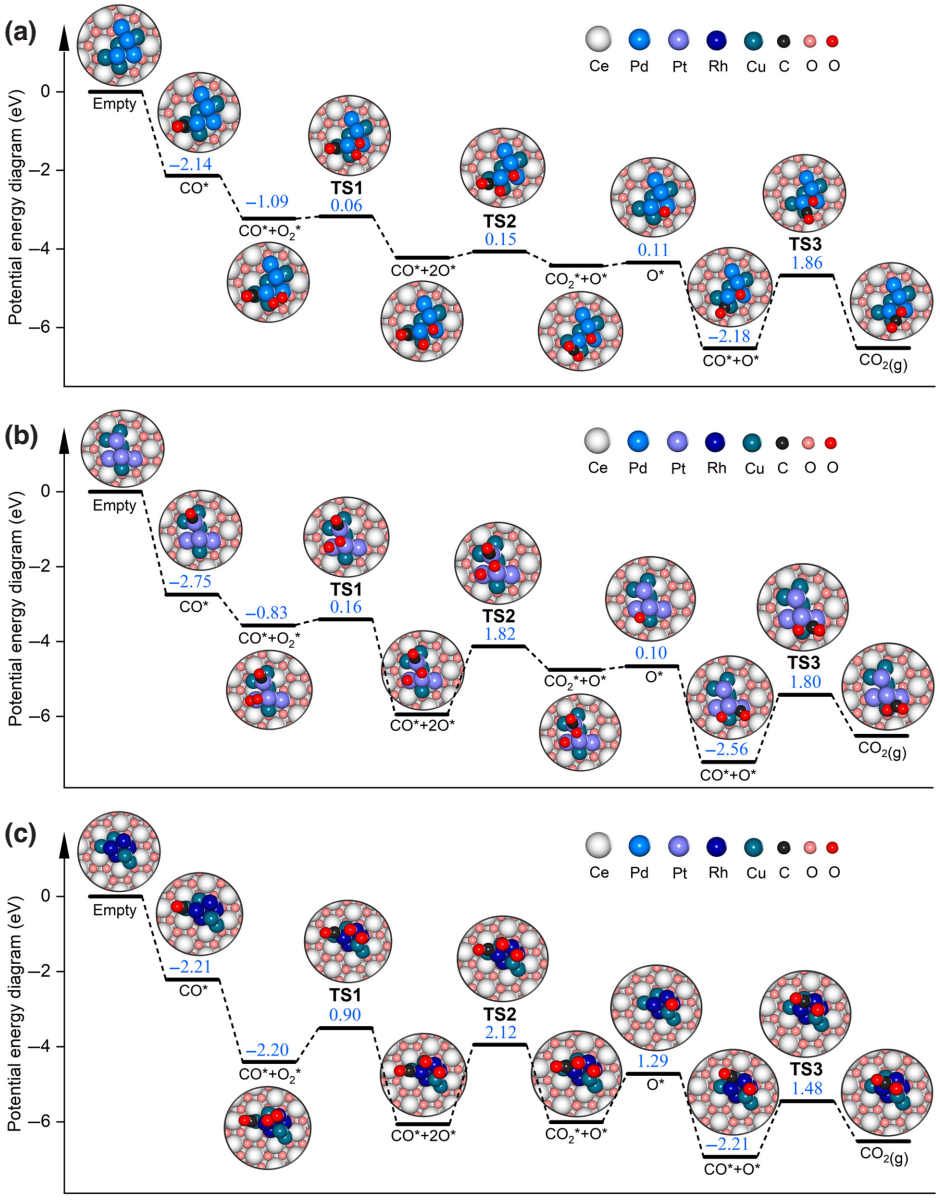

FIG. 3. Potential energy diagrams and corresponding structures for CO oxidation via dissociative pathways on (a) Cu_4Pd_4/CeO_2, (b) Cu_4Pt_4/CeO_2, and (c) Cu_4Rh_4/CeO_2. Key energy profiles and corresponding structures for the reaction via associative pathways on the catalysts are provided in the Supplemental Material [52].

CO oxidation on $Cu_4X_4O_n/CeO_2$ is explored (Fig. 4). The first CO oxidation involves an oxygen atom of $Cu_4X_4O_n$, resulting in an oxygen vacancy on the cluster. This process occurs on $Cu_4Pd_4O_{10}$, $Cu_4Pt_4O_{11}$, and $Cu_4Rh_4O_{14}$ and requires energy barriers of 0.64, 0.22, and 0.71 eV, respectively, to be overcome. The low energy barriers indicate that the first CO oxidation on the oxidized clusters are feasible. Additionally, we investigated the reaction of adsorbed CO with surface lattice oxygen at the interface and found that CO could not bind to the oxygen-saturated Pd sites at the interface. Thus, the following reaction is unfavorable at the $Cu_4Pd_4O_{10}/CeO_2$ interface. The initial CO oxidation at the interfaces of $Cu_4Pt_4O_{11}/CeO_2$ and $Cu_4Rh_4O_{14}/CeO_2$ encounters higher energy barriers than the reaction at the top of the corresponding clusters (Fig. S7 within the Supplemental Material [52]). Therefore, CO oxidation is less likely to take place at the $Cu_4X_4O_n/CeO_2$ interfaces. Therefore, we focus on the study of the reaction pathway for CO oxidation on the clusters. After CO_2 desorption from the cluster, O_2 adsorbs on the vacancy site with moderate adsorption energies, i.e., −1.03 eV ($Cu_4Pd_4O_{10}/CeO_2$), −0.99 eV ($Cu_4Pt_4O_{11}/CeO_2$), and −1.42 eV ($Cu_4Rh_4O_{14}/CeO_2$). In the O_2 dissociative reaction mechanism, molecular

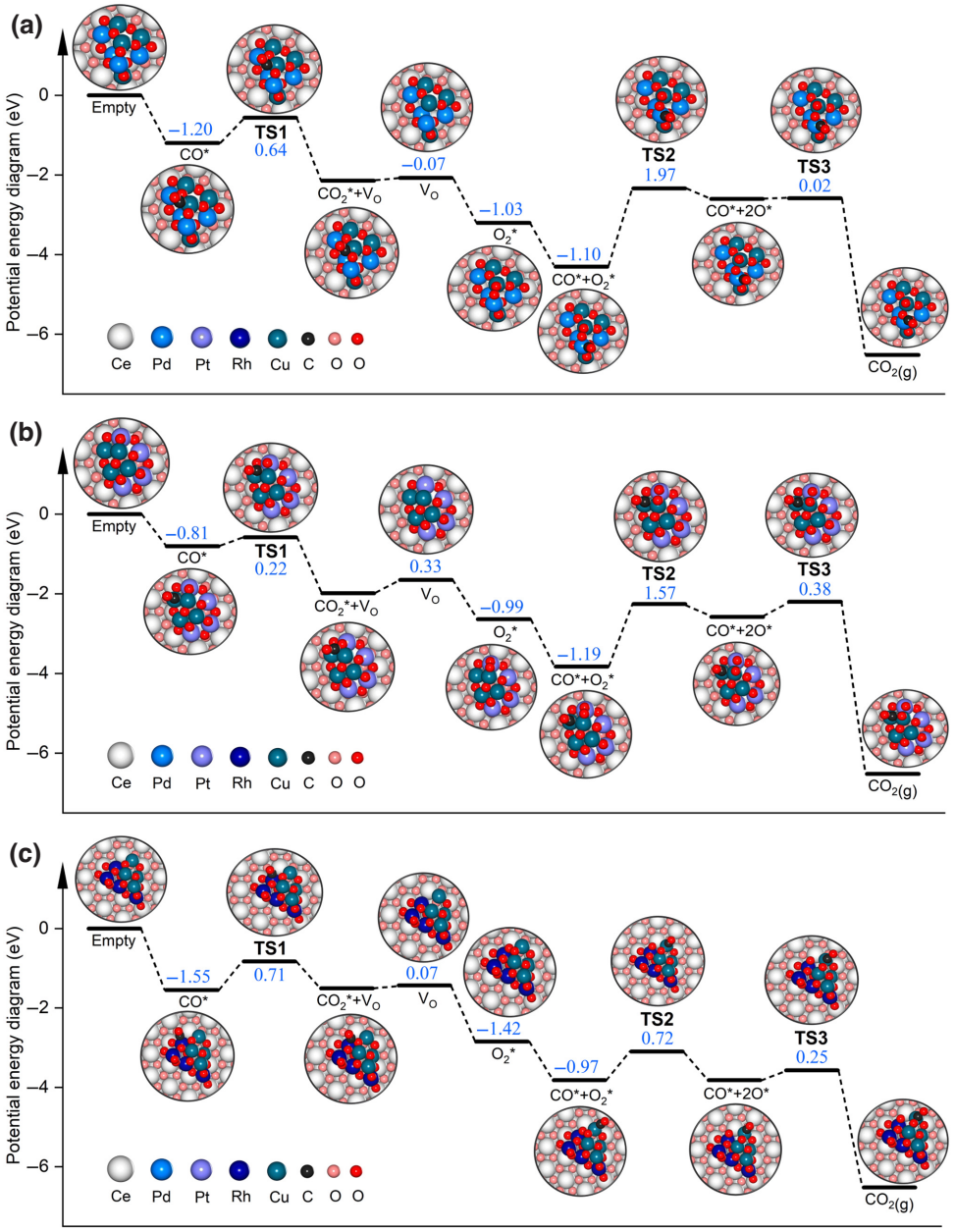

FIG. 4. Potential energy diagrams and corresponding structures for CO oxidation via the O_2 associative pathway on (a) $Cu_4Pd_4O_{10}/CeO_2$, (b) $Cu_4Pt_4O_{11}/CeO_2$, and (c) $Cu_4Rh_4O_{14}/CeO_2$.

O_2 adsorbs on the vacancy site and dissociates on the $Cu_4X_4O_n$ clusters, resulting in healing of the O vacancy and migration of the other O atom to the nearest metal site. The energy barriers for O_2 dissociation on $Cu_4Pd_4O_{10}$ and $Cu_4Pt_4O_{11}$ are as high as 1.97 and 1.57 eV, respectively. A low energy barrier of 0.72 eV is found for the same process on the $Cu_4Rh_4O_{14}$ cluster. Then, the second CO reacts with the O atoms on the $Cu_4X_4O_n$ clusters ($CO_{ads} + O_{ads} \rightarrow CO_2$) to form the second CO_2, which has low energy barriers (Fig. 4). The energy barriers for the $CO_{ads} + O_{2ads} \rightarrow OCOO^*$ step occurring on $Cu_4Pd_4O_{10}$ and $Cu_4Pt_4O_{11}$ are 1.02 and 0.81 eV, respectively, both of which are lower than those for the reaction via the O_2 dissociative pathway (Fig. 4 and Fig. S5 within the Supplemental Material [52]). The energy barrier for the second CO oxidation on the $Cu_4Rh_4O_{14}$ cluster via the O_2 associative reaction pathway is much higher than that in the O_2 dissociative reaction pathway. Hence, CO oxidation takes place on $Cu_4Pd_4O_{10}$ and $Cu_4Pt_4O_{11}$ via the O_2 associative reaction mechanism, whereas the reaction on $Cu_4Rh_4O_{14}$ proceeds via the O_2 dissociative pathway. Additionally, our calculations indicate that Cu_8/CeO_2 would be oxidized

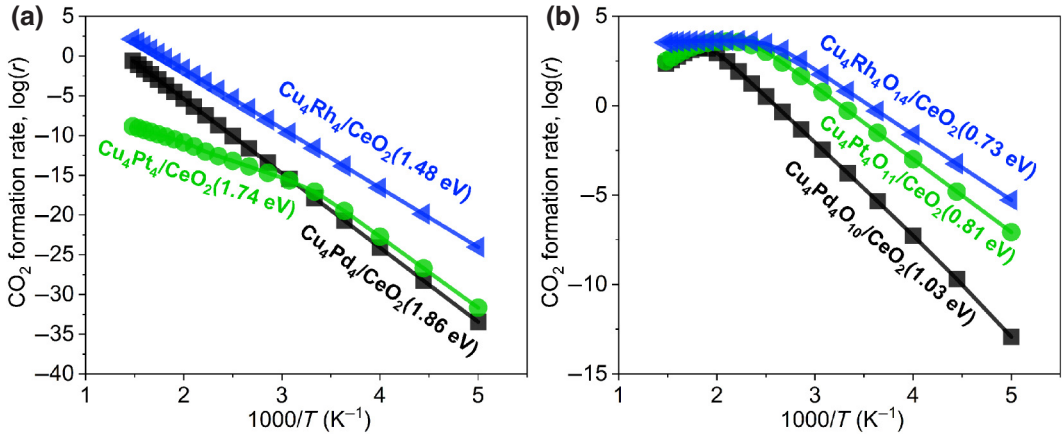

FIG. 5. CO_2 formation rate, r (in mol s^{-1}), as a function of temperature for CO oxidation on different models ($P = 1$ atm, CO : O_2 ratio = 1). (a) Cu_4X_4/CeO_2, (b) $Cu_4X_4O_n/CeO_2$.

to Cu_8O_{11}/CeO_2 in the same oxygen-rich environment. The energy profile for CO oxidation on Cu_8O_{11}/CeO_2 suggests that the reaction via the O_2 dissociative pathway requires a maximum energy barrier of 1.34 eV to be overcome, while the reaction taking place on the cluster via the O_2 associative pathway encounters an energy barrier of 1.12 eV (Figs. S8 and S9 within the Supplemental Material [52]). It is clear that the energy barrier for the rate-determining step on Cu_8O_{11}/CeO_2 is higher than that observed on $Cu_4X_4O_n/CeO_2$. Thus, our calculations suggest that alloying Cu with noble metals can improve the catalytic activity of the clusters. It is worthy of note that the models considered in our study represent typical and possible scenarios, which may exclude the lowest energy barrier of the reaction. Hence, the above findings potentially offer insights into the trends of energy barriers, enabling us to provide a qualitative analysis of CO oxidation on the clusters.

To investigate the kinetic properties of CO oxidation on Cu_4X_4/CeO_2 and $Cu_4X_4O_n/CeO_2$, we carried out microkinetic analysis based on the computed potential energy profiles (Tables S3–S8 within the Supplemental

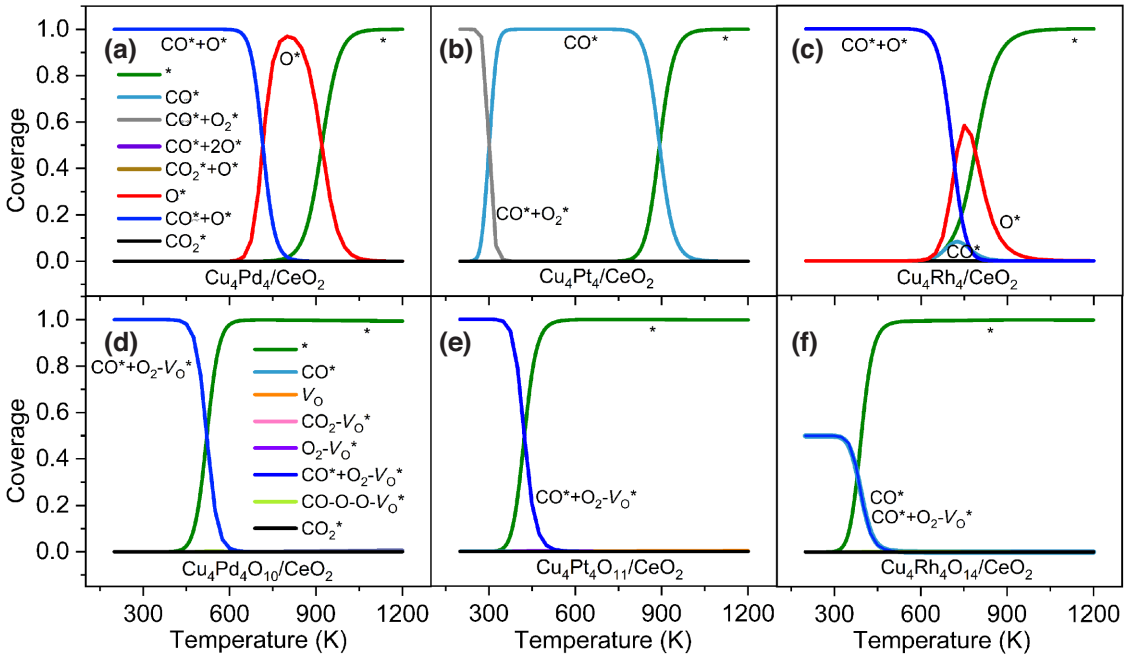

FIG. 6. Steady-state coverage for CO oxidation on (a) Cu_4Pd_4/CeO_2, (b) Cu_4Pt_4/CeO_2, (c) Cu_4Rh_4/CeO_2, (d) $Cu_4Pd_4O_{10}/CeO_2$, (e) $Cu_4Pt_4O_{11}/CeO_2$, and (f) $Cu_4Rh_4O_{14}/CeO_2$. (* represents empty surface sites and V_O stands for oxygen vacancy, $P = 1$ atm, CO : O_2 ratio = 1.)

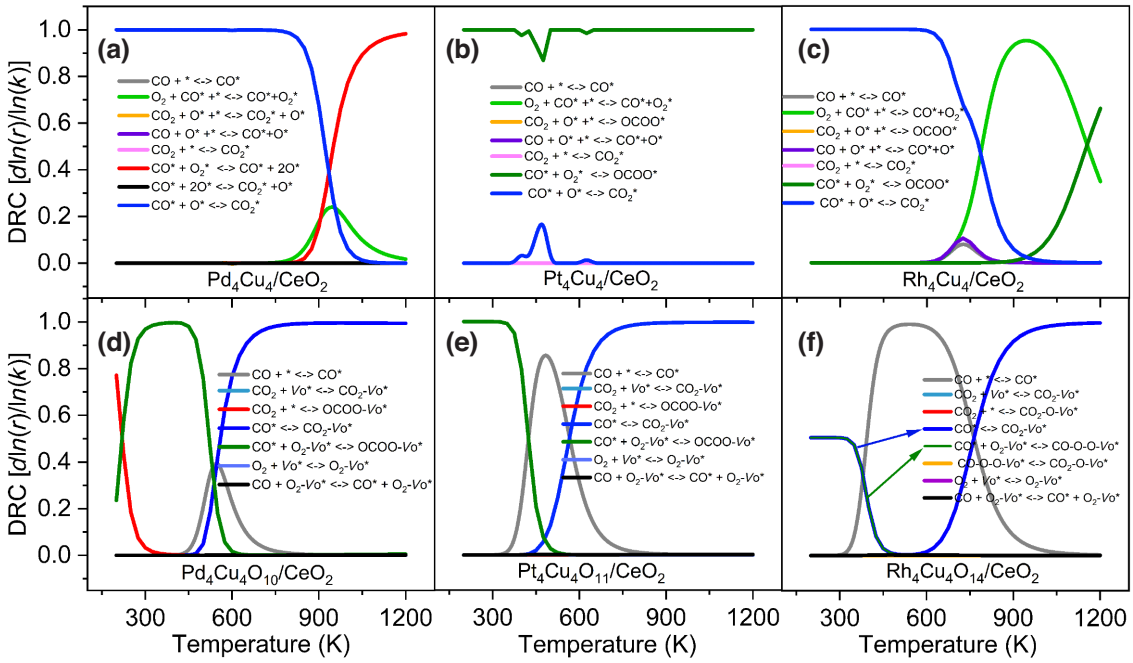

FIG. 7. DRC analysis of CO oxidation on (a) Cu_4Pd_4/CeO_2, (b) Cu_4Pt_4/CeO_2, (c) Cu_4Rh_4/CeO_2, (d) $Cu_4Pd_4O_{10}/CeO_2$, (e) $Cu_4Pt_4O_{11}/CeO_2$, and (f) $Cu_4Rh_4O_{14}/CeO_2$. (* represents empty surface sites and V_O stands for oxygen vacancy, $P = 1$ atm, CO : O_2 ratio = 1.) Elementary reaction steps of the dominant pathways for CO oxidation catalysts are listed.

Material [52]). To simplify our microkinetic modeling, we adopted a CO : O_2 ratio of 1:1 and a total pressure of 1 atm. This assumption allows us to present a qualitative assessment of the catalytic activity of CO oxidation on the clusters. Compared to Cu_4Pd_4/CeO_2 and Cu_4Pt_4/CeO_2, Cu_4Rh_4/CeO_2 has a higher CO oxidation activity, as shown in the Arrhenius curves [Fig. 5(a)]. This is in line with the tendency of the computed apparent activation energies, i.e., 1.86 eV (Cu_4Pd_4/CeO_2), 1.74 eV (Cu_4Pt_4/CeO_2), and 1.48 eV (Cu_4Rh_4/CeO_2). It is worthy of note that $Cu_4X_4O_n/CeO_2$ exhibits a much higher CO oxidation activity than that of Cu_4X_4/CeO_2 [Figs. 5(a) and 5(b)]. Particularly, $Cu_4Rh_4O_{14}/CeO_2$ has the highest activity with the lowest apparent activation energy of 0.73 eV. The above results indicate that the active phase of the supported bimetallic nanocluster has a high oxidation state, resulting in high activity for CO oxidation.

To unravel the underlying kinetics, we further analyzed the steady-state surface coverage and DRCs for the reaction on the catalytic models. Figure 6 shows that Cu_4Pd_4 and Cu_4Rh_4 clusters are occupied by CO and O species at low temperatures. This is consistent with the DRC analysis, which suggests the overall reaction rate for CO oxidation on Cu_4Pd_4 and Cu_4Rh_4 clusters are both controlled by the second CO_2 formation. The Cu_4Pt_4 cluster on CeO_2 is covered by CO and O_2 species at low temperatures. This occurs because adsorbed CO directly reacts with O_2 species via the O_2 associative reaction mechanism, which is the rate-determining step at low temperatures (Fig. 7). The surface coverage and DRC for $Cu_4X_4O_n/CeO_2$ are different from those of Cu_4X_4/CeO_2 due to the different reaction mechanism. At temperatures below 450 K, the metal sites and O vacancy sites of $Cu_4Pd_4O_{10}$ are fully occupied by the CO and O_2 species, respectively. The DRC analysis supports the coverage distribution that adsorbed CO reacting with O_2 species controls the reaction rate. As the temperature increases, the energy barrier for this step can be overcome. Therefore, the coverage of CO and O_2 species decreases as the temperature increases. This process becomes more favorable on $Cu_4Pt_4O_{11}/CeO_2$ due to the lower energy barrier. As a result, the CO and O_2 species start to be converted into $OCOO^*$ species at temperatures above 350 K. $Cu_4Rh_4O_{14}/CeO_2$ is more active and can start to consume adsorbed CO and O_2 species at a lower temperature (325 K). A DRC analysis suggests that the reaction of adsorbed CO with O on the cluster, together with adsorbed O_2 dissociation, controls the overall reaction rate at low temperatures [Fig. 7(f)]. The above results indicate that the rate-determining step for CO oxidation depends on the composition and oxidation state of supported alloy clusters. In our microkinetic simulations, we adopted a mean-field approximation, which assumed a uniform sample with a random distribution of reactants and intermediates on homogeneous clusters. We applied the same approximation for the microkinetic simulations on all the supported clusters. Although the inhomogeneity of the surface sites is not included in our simulations, which may result in a higher reaction rate, the activity

trend of the supported bimetallic clusters is not changed in our study. Therefore, the approximation does not affect qualitative conclusions drawn from the results.

IV. CONCLUSION

We systematically explore the atomic structures and properties of ceria-supported Cu-based bimetallic clusters in an oxygen-rich environment. Using GA and GCMC methods combined with first-principles calculations, our study reveals that the Cu_4Pd_4, Cu_4Pt_4, and Cu_4Rh_4 clusters supported on $CeO_2(111)$ are oxidized to form $Cu_4Pd_4O_{10}$, $Cu_4Pt_4O_{11}$, and $Cu_4Rh_4O_{14}$ clusters under catalytic conditions. The oxidized alloy clusters exhibit a moderate adsorption strength for CO compared to the metallic clusters. Microkinetic simulations suggest that CO oxidation prefers to take place on the oxidized cluster, and the reaction mechanisms vary with the composition of the alloy catalyst. In terms of catalytic activity, the oxidized alloy clusters have much higher CO_2 formation rates than those of the pristine bimetallic clusters. The oxidized alloy clusters on ceria serve as the active sites for CO oxidation rather than their interfaces. The reaction on $Cu_4Pd_4O_{10}$ and $Cu_4Pt_4O_{11}$ clusters proceeds via the O_2 associative reaction mechanism, while CO oxidation on $Cu_4Rh_4O_{14}$ is more favorable through the O_2 dissociative mechanism. Among these catalysts, the ceria-supported $Cu_4Rh_4O_{14}$ nanocluster exhibits the highest activity, consistent with the lowest predicted apparent activation energy (0.73 eV). Our findings demonstrate the structural and catalytic properties of Cu-based bimetallic clusters in an oxygen-rich environment, providing guidance for designing oxide-supported alloy catalysts.

ACKNOWLEDGMENTS

This work was supported by the National Natural Science Foundation of China (Grants No. 22203105, No. 11874429, and No. 12174450); the Hunan Provincial Natural Science Foundation of China (Grant No. 2023JJ40713); the National Talents Program of China, Distinguished Youth Foundation of Hunan Province (Grant No. 2020JJ2039); Hunan Provincial Key Research and Development Program (Grant No. 2022WK2002); the Project of High-Level Talents Accumulation of Hunan Province (Grant No. 2018RS3021); and the Program of Hundreds of Talents of Hunan Province, State Key Laboratory of Powder Metallurgy, Start-up Funding and Innovation-Driven Plan (Grant No. 2019CX023) of Central South University. Fundamental Research Funds for the Central Universities of Central South University (2023ZZTS0386). E.J.M.H. acknowledges financial support from a NWO Vici personal grant. The supercomputing facilities used in the calculations were supported by the NWO. Calculations and simulations were also performed at the High-Performance Computing facilities of Central South University. We thank Dr. Ming-Wen Chang for useful discussions.

The authors declare no conflict of interest.

[1] Z. Jia, M. Peng, X. Cai, Y. Chen, X. Chen, F. Huang, L. Zhao, J. Diao, N. Wang, and D. Xiao, Fully exposed platinum clusters on a nanodiamond/graphene hybrid for efficient low-temperature CO oxidation, ACS Catal. **12**, 9602 (2022).

[2] S. Ji, Y. Chen, Q. Fu, Y. Chen, J. Dong, W. Chen, Z. Li, Y. Wang, L. Gu, and W. He, Confined pyrolysis within metal–organic frameworks to form uniform Ru_3 clusters for efficient oxidation of alcohols, J. Am. Chem. Soc. **139**, 9795 (2017).

[3] L. Yang, G. Li, R. Ma, S. Hou, J. Chang, M. Ruan, W. Cai, Z. Jin, W. Xu, G. Wang, J. Ge, C. Liu, and W. Xing, Nanocluster PtNiP supported on graphene as an efficient electrocatalyst for methanol oxidation reaction, Nano Res. **14**, 2853 (2021).

[4] J.-C. Liu, X.-L. Ma, Y. Li, Y.-G. Wang, H. Xiao, and J. Li, Heterogeneous Fe_3 single-cluster catalyst for ammonia synthesis via an associative mechanism, Nat. Commun. **9**, 1610 (2018).

[5] X. Liu, S. Jia, M. Yang, Y. Tang, Y. Wen, S. Chu, J. Wang, B. Shan, and R. Chen, Activation of subnanometric Pt on Cu-modified CeO_2 via redox-coupled atomic layer deposition for CO oxidation, Nat. Commun. **11**, 4240 (2020).

[6] L. Zhang, G. Spezzati, V. Muravev, M. A. Verheijen, B. Zijlstra, I. A. Filot, Y.-Q. Su, M.-W. Chang, and E. J. Hensen, Improved Pd/CeO_2 catalysts for low-temperature NO reduction: Activation of CeO_2 lattice oxygen by Fe doping, ACS Catal. **11**, 5614 (2021).

[7] Y. Wang, D. Wu, T. Liu, G. Liu, and X. Hong, Fabrication of PdZn alloy catalysts supported on ZnFe composite oxide for CO_2 hydrogenation to methanol, J. Colloid Interface Sci. **597**, 260 (2021).

[8] C. Dong, Z. Gao, Y. Li, M. Peng, M. Wang, Y. Xu, C. Li, M. Xu, Y. Deng, and X. Qin, Fully exposed palladium cluster catalysts enable hydrogen production from nitrogen heterocycles, Nat. Catal. **5**, 485 (2022).

[9] P. Poldorn, Y. Wongnongwa, S. Namuangruk, N. Kungwan, V. B. Golovko, B. Inceesungvorn, and S. Jungsuttiwong, Theoretical mechanistic study of CO catalytic oxidation by O_2 on an ultra-small 13-atom bimetallic Ag_7Au_6 cluster, Appl. Catal., A **595**, 117505 (2020).

[10] L.-J. Zuo, S.-L. Xu, A. Wang, P. Yin, S. Zhao, and H.-W. Liang, High-temperature synthesis of carbon-supported bimetallic nanocluster catalysts by enlarging the interparticle distance, Inorg. Chem. **61**, 2719 (2022).

[11] X. Zhang, R. Yan, W. Zhou, and S. Zhou, Pt-Ru bimetallic nanoparticles anchored on carbon nanotubes/polyaniline composites with coral-like structure for enhanced methanol oxidation, J. Alloys Compd. **920**, 165990 (2022).

[12] J. Zhao and R. Jin, Heterogeneous catalysis by gold and gold-based bimetal nanoclusters, Nano Today **18**, 86 (2018).

[13] W. Zhan, J. Wang, H. Wang, J. Zhang, X. Liu, P. Zhang, M. Chi, Y. Guo, Y. Guo, and G. Lu, Crystal structural effect of AuCu alloy nanoparticles on catalytic CO oxidation, J. Am. Chem. Soc. **139**, 8846 (2017).

[14] N. Jain, A. Roy, and S. Nair, Reduced $SrTiO_3$-supported Pt-Cu alloy nanoparticles for preferential oxidation of CO in excess hydrogen, Nanoscale **11**, 22423 (2019).

[15] M. Zheng, C. Jia, E. Sharman, J. Jiang, W. Fan, and X. Zhao, Maximizing the synergistic effect of PdAu catalysts on $TiO_2(101)$ for robust CO_2 reduction: A DFT study, Appl. Surf. Sci. **563**, 150365 (2021).

[16] L. Ma, K. Laasonen, and J. Akola, Catalytic activity of AuCu clusters on MgO (100): Effect of alloy composition for CO oxidation, J. Phys. Chem. C **121**, 10876 (2017).

[17] X. Liu, A. Wang, L. Li, T. Zhang, C.-Y. Mou, and J.-F. Lee, Structural changes of Au-Cu bimetallic catalysts in CO oxidation: *In situ* XRD, EPR, XANES, and FT-IR characterizations, J. Catal. **278**, 288 (2011).

[18] D. Wu, R. Jia, M. Wen, S. Zhong, Q. Wu, Y. Fu, and S. Yu, Ultrastable $PtCo/Co_3O_4 - SiO_2$ nanocomposite with active lattice oxygen for superior catalytic activity toward CO oxidation, Inorg. Chem. **59**, 1218 (2019).

[19] P. Destro, T. M. Kokumai, A. Scarpellini, L. Pasquale, L. Manna, M. Colombo, and D. Zanchet, The crucial role of the support in the transformations of bimetallic nanoparticles and catalytic performance, ACS Catal. **8**, 1031 (2018).

[20] W. Song, L. Chen, L. Wan, M. Jing, and Z. Li, The influence of doping amount on the catalytic oxidation of formaldehyde by Mn-CeO_2 mixed oxide catalyst: A combination of DFT and microkinetic study, J. Hazard. Mater. **425**, 127985 (2022).

[21] W. Song, L. Chen, J. Deng, M. Jing, H. Zheng, J. Liu, and Z. Zhao, Combination of density functional theory and microkinetic study to the Mn-doped CeO_2 catalysts for CO oxidation: A case study to understand the doping metal content, J. Phys. Chem. C **122**, 25290 (2018).

[22] Q. Wan, F. Wei, Y. Wang, F. Wang, L. Zhou, S. Lin, D. Xie, and H. Guo, Single atom detachment from Cu clusters, and diffusion and trapping on $CeO_2(111)$: Implications in Ostwald ripening and atomic redispersion, Nanoscale **10**, 17893 (2018).

[23] X. Liao, Y. Liu, W. Chu, S. Sall, C. Petit, V. Pitchon, and V. Caps, Promoting effect of AuCu alloying on Au-Cu/CeO_2-catalyzed CO oxidation: A combined kinetic and *in situ* DRIFTS study, J. Catal. **382**, 329 (2020).

[24] S. Monyanon, S. Pongstabodee, and A. Luengnaruemitchai, Catalytic activity of Pt-Au/CeO_2 catalyst for the preferential oxidation of CO in H_2-rich stream, J. Power Sources **163**, 547 (2006).

[25] X. Zhang, J.-X. Liu, B. Zijlstra, I. A. Filot, Z. Zhou, S. Sun, and E. J. Hensen, Optimum Cu nanoparticle catalysts for CO_2 hydrogenation towards methanol, Nano Energy **43**, 200 (2018).

[26] L. Zhang, H. Y. Kim, and G. Henkelman, CO oxidation at the Au-Cu interface of bimetallic nanoclusters supported on $CeO_2(111)$, J. Phys. Chem. Lett. **4**, 2943 (2013).

[27] Y. Liu, H. Li, W. Cen, J. Li, Z. Wang, and G. Henkelman, A computational study of supported Cu-based bimetallic nanoclusters for CO oxidation, Phys. Chem. Chem. Phys. **20**, 7508 (2018).

[28] B. Liu, Z. Zhao, G. Henkelman, and W. Song, Computational design of a CeO_2-supported Pd-based bimetallic nanorod for CO oxidation, J. Phys. Chem. C **120**, 5557 (2016).

[29] J.-X. Liu, Y. Su, I. A. Filot, and E. J. Hensen, A linear scaling relation for CO oxidation on CeO_2-supported Pd, J. Am. Chem. Soc. **140**, 4580 (2018).

[30] M.-W. Chang, L. Zhang, M. Davids, I. A. Filot, and E. J. Hensen, Dynamics of gold clusters on ceria during CO oxidation, J. Catal. **392**, 39 (2020).

[31] P. E. Blöchl, Projector augmented-wave method, Phys. Rev. B **50**, 17953 (1994).

[32] G. Kresse and J. Furthmüller, Efficient iterative schemes for *ab initio* total-energy calculations using a plane-wave basis set, Phys. Rev. B **54**, 11169 (1996).

[33] G. Kresse and J. Hafner, *Ab initio* molecular dynamics for liquid metals, Phys. Rev. B **47**, 558 (1993).

[34] J. P. Perdew, K. Burke, and M. Ernzerhof, Generalized Gradient Approximation Made Simple, Phys. Rev. Lett. **77**, 3865 (1996).

[35] S. Fabris, S. de Gironcoli, S. Baroni, G. Vicario, and G. Balducci, Taming multiple valency with density functionals: A case study of defective ceria, Phys. Rev. B **71**, 041102 (2005).

[36] G. Henkelman, B. P. Uberuaga, and H. Jónsson, A climbing image nudged elastic band method for finding saddle points and minimum energy paths, J. Chem. Phys. **113**, 9901 (2000).

[37] T. P. Senftle, R. J. Meyer, M. J. Janik, and A. C. Van Duin, Development of a ReaxFF potential for Pd/O and application to palladium oxide formation, J. Chem. Phys. **139**, 044109 (2013).

[38] L. Gai, Y. K. Shin, M. Raju, A. C. Van Duin, and S. Raman, Atomistic adsorption of oxygen and hydrogen on platinum catalysts by hybrid grand canonical Monte Carlo/reactive molecular dynamics, J. Phys. Chem. C **120**, 9780 (2016).

[39] P. Linstrom and W. Mallard, The NIST chemistry webbook: A chemical data resource on the internet, J. Chem. Eng. Data **46**, 1059 (2001).

[40] A. P. J. Jansen, *An introduction to kinetic Monte Carlo simulations of surface reactions* (Springer, Berlin, 2012).

[41] P. W. Atkins and J. De Paula, *Physical Chemistry* (Oxford University Press, London, 2018).

[42] I. A. Filot, R. A. Van Santen, and E. J. Hensen, The optimally performing Fischer–Tropsch catalyst, Angew. Chem. Int. Ed. **53**, 12746 (2014).

[43] C. T. Campbell, Future directions and industrial perspectives micro-and macro-kinetics: Their relationship in heterogeneous catalysis, Top. Catal. **1**, 353 (1994).

[44] C. T. Campbell, Finding the rate-determining step in a mechanism: Comparing DeDonder relations with the "degree of rate control", J. Catal. **204**, 520 (2001).

[45] I. A. W. Filot, B. Zijlstra, E. J. M. Hensen, and MKMCXX, A C++ program for constructing microkinetic models. http://www.mkmcxx.nl

[46] P. N. Brown, G. D. Byrne, and A. C. Hindmarsh, VODE: A variable-coefficient ODE solver, SIAM J. Comput. **10**, 1038 (1989).

[47] G. D. Byrne and A. C. Hindmarsh, A polyalgorithm for the numerical solution of ordinary differential equations, ACM Trans. Math. Softw. **1**, 71 (1975).

[48] G. D. Byrne and A. C. Hindmarsh, Stiff ODE solvers: A review of current and coming attractions, J. Comput. Phys. **70**, 1 (1987).

[49] B. Yoon, H. Hakkinen, U. Landman, A. S. Worz, J.-M. Antonietti, S. Abbet, K. Judai, and U. Heiz, Charging effects on bonding and catalyzed oxidation of CO on Au_8 clusters on MgO, Science **307**, 403 (2005).

[50] L. Martínez-Suárez, J. Frenzel, D. Marx, and B. Meyer, Tuning the Reactivity of a Cu/ZnO Nanocatalyst via Gas Phase Pressure, Phys. Rev. Lett. **110**, 086108 (2013).

[51] M. Chen and D. Goodman, The structure of catalytically active gold on titania, Science **306**, 252 (2004).

[52] See the Supplemental Material at http://link.aps.org/supplemental/10.1103/PhysRevApplied.20.034051 for more details of PDOS analyses, optimized configurations, adsorption energies of CO, potential energy diagrams, elementary reaction steps, and relevant energies used in the microkinetic modelling.